**PASJ:** Publ. Astron. Soc. Japan **63**, S635–S644, 2011 November 25


# In-Orbit Performance of MAXI Gas Slit Camera (GSC) on ISS

Mutsumi SUGIZAKI,[1] Tatehiro MIHARA,[1] Motoko SERINO,[1] Takayuki YAMAMOTO,[1,5] Masaru MATSUOKA,[1,2] Mitsuhiro KOHAMA,[2] Hiroshi TOMIDA,[2] Shiro UENO,[2] Nobuyuki KAWAI,[3] Mikio MORII,[3] Kousuke SUGIMORI,[3] Satoshi NAKAHIRA,[4] Kazutaka YAMAOKA,[4] Atsumasa YOSHIDA,[4] Motoki NAKAJIMA,[5] Hitoshi NEGORO,[5] Satoshi EGUCHI,[6] Naoki ISOBE,[6] Yoshihiro UEDA,[6] and Hiroshi TSUNEMI[7]

[1]*MAXI team, RIKEN, 2-1 Hirosawa, Wako, Saitama 351-0198*
*sugizaki@riken.jp*
[2]*ISS Science Project Office, ISAS, JAXA, 2-1-1 Sengen, Tsukuba, Ibaraki 305-8505*
[3]*Department of Physics, Tokyo Institute of Technology, 2-12-1 Ookayama, Meguro-ku, Tokyo 152-8551*
[4]*Department of Physics and Mathematics, Aoyama Gakuin University, 5-10-1 Fuchinobe, Chuo-ku, Sagamihara 229-8558*
[5]*Department of Physics, Nihon University, 1-8-14, Kanda-Surugadai, Chiyoda-ku, Tokyo 101-8308*
[6]*Department of Astronomy, Kyoto University, Kitashirakawa Oiwake-cho, Sakyo-ku, Kyoto 606-8502*
[7]*Department of Earth and Space Science, Osaka University, 1-1 Machikaneyama, Toyonaka, Osaka 560-0043*

(Received 2010 November 1; accepted 2011 February 1)

**Abstract**

We report on the in-orbit performance of the Gas Slit Camera (GSC) on the MAXI (Monitor of All-sky X-ray Image) mission carried on the International Space Station (ISS). Its commissioning operation, which started on 2009 August 8, confirmed the basic performances of the effective area in the energy band of 2–30 keV, the spatial resolution of the slit-and-slat collimator and detector with 1.°5 FWHM, the source visibility of 40–150 seconds for each scan cycle, and the sky coverage of 85% per 92-minute orbital period and 95% per day. The gas gains and read-out amplifier gains have been stable within 1%. The background rate is consistent with the past X-ray experiments operated at a similar low-earth orbit if its relation with the geomagnetic cutoff rigidity is extrapolated to high latitude. We also present the status of the in-orbit operation and a calibration of the effective area and the energy response matrix using Crab-nebula data.

**Key words:** instrumentation: detectors — X-rays: general — X-rays: individual (Crab Nebula)

## 1. Introduction

MAXI (Monitor of All-sky X-ray Image) is the first astronomical mission operated on the ISS (International Space Station) (Matsuoka et al. 2009). The payload was delivered to the ISS by Space Shuttle Endeavour on 2009 July 16, and installed on the Japanese Experiment Module — Exposed Facility (JEM-EF or Kibo-EF) on July 24. The mission was designed to achieve the best sensitivity and the highest energy resolution among the all-sky X-ray monitors performed so far by using two kinds of X-ray slit cameras, Gas Slit Camera (GSC: Mihara et al. 2011) and Solid-state Slit Camera (SSC: Tomida et al. 2011), which work in complementary way.

The GSC is the main X-ray camera to cover the energy band from 2 to 30 keV with a large area. It employs a conventional slit camera that consists of Xe-gas proportional counters and slit-and-slat collimators. Twelve gas counters achieve a large detector area of 5350 $cm^2$. They are assembled into six identical units to cover wide fields of views (FOVs) of 1.°5 $\times$ 160°. They are embodied in the MAXI payload module, such that they cover the Earth-horizon and the zenith directions with an equal area. This enables us to cover the entire sky every 92-minute orbital period, even if the GSC has to be partly downed in a heavy particle-radiation environment, such as the passage of the SAA (South Atlantic Anomaly). The Xe-gas counters employ resistive carbon-wire anodes to acquire one-dimensional position sensitivity. The gas volume of each counter is separated into six carbon-anode cells for the main X-ray detectors and ten tungsten-anode cells for veto counters. The veto cells surround the carbon-anode cells so as to reduce backgrounds by the anti-coincidence-hit logic. A total of 14 anode signals in each counter are read out independently through an electronics unit, and processed by on-board data processors. Figure 1 illustrates schematic views of a single GSC camera unit and FOVs of all six units on the ISS low-earth orbit. The details of the instruments are described in Mihara et al. (2011).

This paper presents the GSC in-orbit performance, including the operation and calibration status. The SSC in-orbit performance is presented in Tsunemi et al. (2010).

## 2. Operation

### 2.1. Initial Operation

The main power of the MAXI payload is supplied from the JEM-EF via the Payload Interface Unit (PIU). It was activated on August 3, one week after the payload was installed on the JEM-EF. On August 4, the GSC electronics units (GSC-E) including the Radiation-Belt Monitor (RBM) were switched on. The on-board RBM parameters, thresholds of the lower discriminators and count-rate criteria to down the gas counters, were then set up using data taken for the first three days. On August 8, the high voltage of the first gas counter was activated and increased up to the nominal operation voltage of 1650 V.

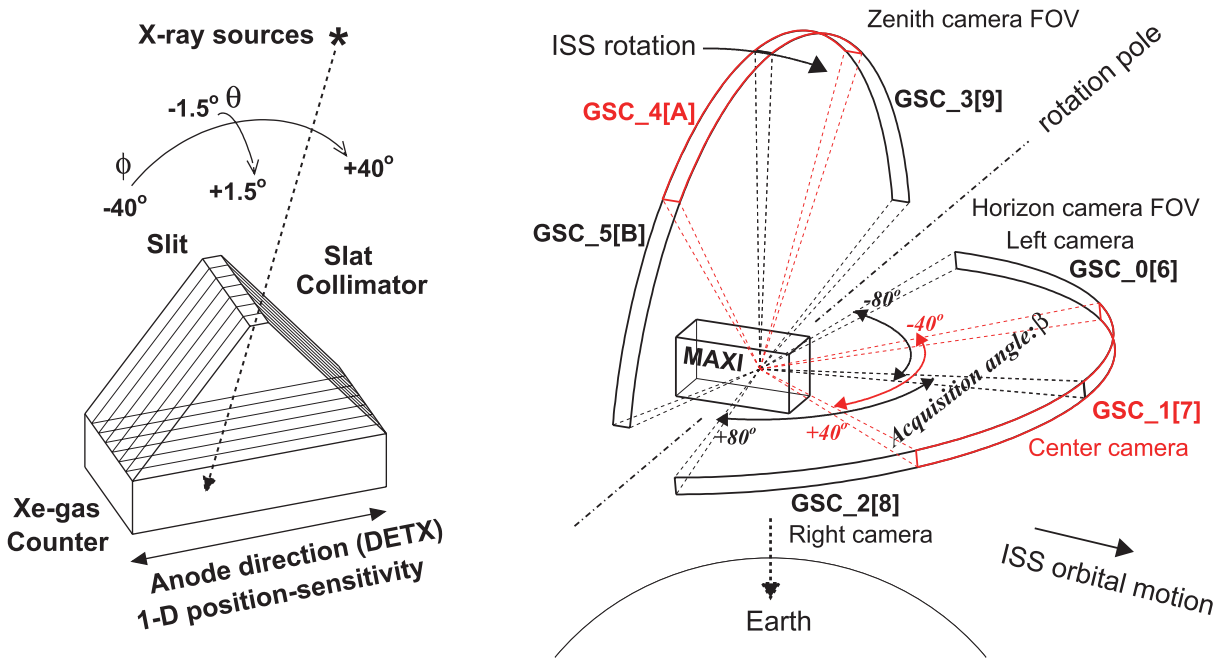


**Fig. 1.** (Left) Schematic view of a single GSC camera unit and its field of view (FOV) of 1.°5 (FWHM) × 80°. (Right) FOVs of the six camera units including 12 counters (GSC_0, ..., GSC_9, GSC_A, GSC_B) on the ISS low-earth orbit. Every two counters, such as GSC_0 and GSC_6, are used as a pair for a redundancy. Left, center, and right camera units cover the area of source-acquisition angle $\beta$ of $-80° < \beta < 0°$, $-40° < \beta < +40°$, and $0° < \beta < +80°$, respectively.

The first test observation was then performed for three hours and various analog/digital-electronic functions were verified. All of the 12 counters were activated at the nominal 1650 V since August 10 to 13 one by one.

Each gas counter has 14 anode signals for both two ends of six carbon-wire anodes and two veto signals. Each anode signal has an individual pre-amplifier, a shaping amplifier, a lower discriminator (LD), and an Analog-to-Digital Converter (ADC) which produces a 14-bit pulse height. The gain of the shaping amplifier and the threshold of the lower discriminator of each signal can be changed by command. These parameters are adjusted according to the gas gain of individual anode wires. The first all-sky image by all 12 counters was taken on August 15.

### 2.2. *RBM*

GSC incorporates Radiation-Belt Monitor (RBM) to monitor the flux of the cosmic rays in orbit. Two silicon-PIN-diode detectors with 0.2-mm thickness and $5 \times 5\,\mathrm{mm}^2$ area are equipped with each of GSC horizon and zenith center units. The detector on the horizon unit (RBM-H) is faced to tangential direction of the ISS motion along the Earth horizon. The zenith unit (RBM-Z) is faced perpendicular to the horizontal plane. The RBMs always monitor the count rates of cosmic rays with a certain energy deposit, whose threshold can be changed by commands. The level of the threshold is set at 50 keV, which corresponds to half of the minimum ionization-loss energy of the relativistic particles.

Figure 2 shows the RBM count-rate maps on the ISS orbital area by RBM-H and RBM-Z units, respectively, averaged over the data taken for the first year. The ratio of the RBM-H to the RBM-Z count rate is shown at the bottom where contours of the inclination angle of the magnetic field from the Earth-horizontal plane are overlaid. The two RBM rates agree with each other in the low count-rate area below 0.2 Hz, where the anti-correlations with the geomagnetic cutoff rigidity (COR) are clearly seen. It indicates that the origins are energetic cosmic rays. The cosmic-ray flux $\sim 1\,\mathrm{counts\,cm^{-2}\,s^{-1}}$ and its relation with the COR are consistent with those obtained by ASCA (Makishima et al. 1996) and Suzaku (Kokubun et al. 2007) in low-earth orbit although the altitude of the ISS, 340–360 km, is different from that of these satellites, 530–590 km.

While the two RBM rates agreed at the low-radiation area, they are quite different in the high-radiation area around the SAA, and both geomagnetic poles are located north of the north American continent and south of the Australian continent. The RBM-H rate is higher by an order of magnitude than the RBM-Z rate in these areas. From the correlation between their ratio and the inclination of the magnetic field, the difference is considered to be due to the anisotropy of the flux of trapped particles. A large number of cosmic-ray particles trapped by the geomagnetic fields are moving circularly on the horizontal plane around the magnetic pole. The RBM-Z detector faced on the zenith direction is insensitive to the particles moving on the horizontal plane. The anisotropy of the trapped particles at high latitude has also been recognized by images of particle tracks taken by the SSC CCD imager (Tsunemi et al. 2010).

### 2.3. *High Voltage Operation*

We started full GSC operation with twelve counter units (GSC_0, ..., GSC_9, GSC_A, GSC_B) on 2009 August 15.

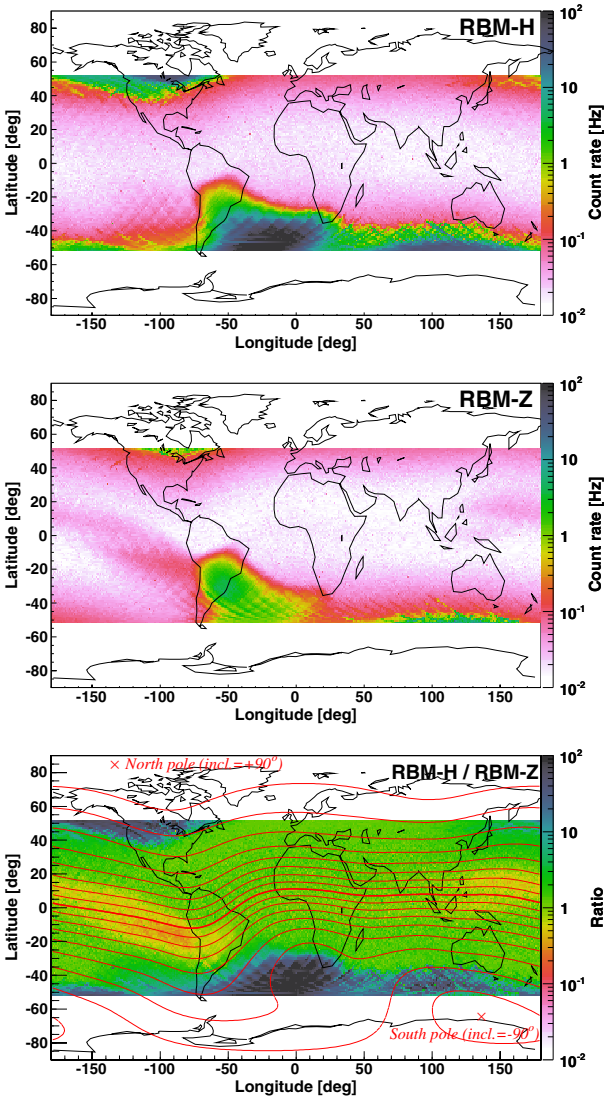


**Fig. 2.** RBM count-rate maps of horizon (RBM-H, top panel) and zenith (RBM-Z, middle panel) units. Bottom panel shows their ratio (RBM-H / RBM-Z) and contours of the inclination angle of the magnetic fields from the horizontal plane are drawn by 10° step from −90° (south pole) to 90° (north pole).

The high voltages of all twelve gas counters were set at the nominal 1650 V. They are reduced to 0 V when the ISS passes through heavy particle background area, defined by an on-board Radiation-Zone (RZ) map. At the beginning of the mission, we set the RZ map only at the SAA.

On 2009 September 8, the analog power on the GSC_6 counter was suddenly down. It was followed by power down of another counter, GSC_9, on September 14. The data indicate that a carbon-anode wire in each of these counters was fractured. It was also suggested that the location fractured on the carbon wire would be where a large amount of discharges occurred repeatedly.

We then changed the counter operation strategy so that any risks to cause potential damages on the carbon-anode wire, such as discharge and heavy irradiation, should be avoided as much as possible. High-voltage reduction at high latitudes above 40° was employed since September 23. Two noisy counters, GSC_A and GSC_B, which are considered to have been fractured sooner, were also tentatively stopped on September 26.

On 2010 March 26, the analog power on the GSC_3 counter was downed, which was considered to be due to a carbon-wire fracture by a breakdown discharge again. Since then, the operation voltage was reduced to 1550 V if the counter had any discharge experience.

As results of these limited HV operations, the effective observation efficiency has been reduced to about 40%. It is expected to reduce the sensitivity. The three counters suffering from the breakdown will be soon activated with great care.

## 3. In-Orbit Performance

### *3.1. Background*

The GSC counter has a one-dimensional position sensitivity, and performs scanning observations. Backgrounds for any X-ray sources on the sky can be roughly estimated from the levels of the adjacent source-free region. Studies of the backgrounds are important because the residual backgrounds and their uncertainties limit the source-detection sensitivity.

#### *3.1.1. LD-hit rate and processed event rate*

Each GSC gas counter embodies six carbon-anode cells for the main X-ray detector and veto cells surrounding the carbon-anode cells. The cosmic-ray backgrounds are screened out on board by applying an anti-coincidence matrix to the hit patterns of all anode signals in each counter. The efficiency of the background reduction depends on the LD threshold of the read-out signals. The amplifier gains and LD levels of all the read-out signals are tuned during the initial verification operation.

The background rates of all the 12 GSC counters are found to have a similar time variation during the entire observation-operation period. They exhibit clear anti-correlations with the geomagnetic COR in orbit. Figure 3 illustrates the LD-hit rate, the processed event rate after the anti-coincidence cut, and the cleaned event rate with the PHA (Pulse-Height Amplitude) range of the 2–30 keV energy band against the COR. Each data point represents the rate per anode averaged over six anodes in a counter, GSC_0, every minute, taken for a day on 2009 August 18, except while the ISS is in a heavy particle-irradiation area detected by an RBM and RZ map. Data expected to include significant X-ray events from celestial bright X-ray sources are also excluded. The ratio of the anti-coincidence-event rate to the LD-hit rate is about 1 : 30, and almost constant over the entire period. This is quite similar to the Ginga-LAC case (Turner et al. 1989). The LD-hit rate well agrees with the RBM rate, taking the detector area, 90 $cm^2$ per anode, into account. This indicates that they are of energetic cosmic-ray origin.

#### *3.1.2. Energy spectrum*

Figure 4 shows the energy spectra of the residual backgrounds sorted by COR and the estimated contribution of the unresolved Cosmic X-ray Background (CXB) within the FOV (e.g., Gendreau et al. 1995). The profile shows the fluorescent lines of Ti-K at 4.6 keV from the gas-counter body and Cu-K at 8.1 keV from the slat collimator made of phosphor bronze. These emission lines are used for energy response calibration.

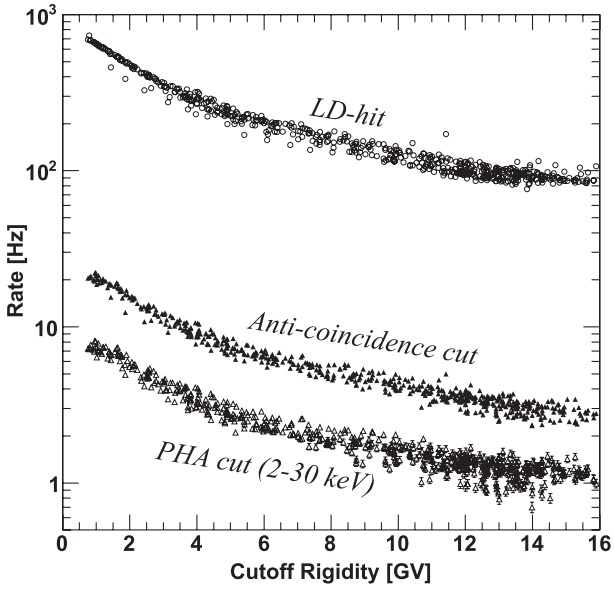


**Fig. 3.** GSC LD-hit rate, on-board processed event rate after an anti-coincidence cut, and PHA-filtered event rate with an energy band of 2–30 keV per anode cell against the geomagnetic cutoff rigidity.

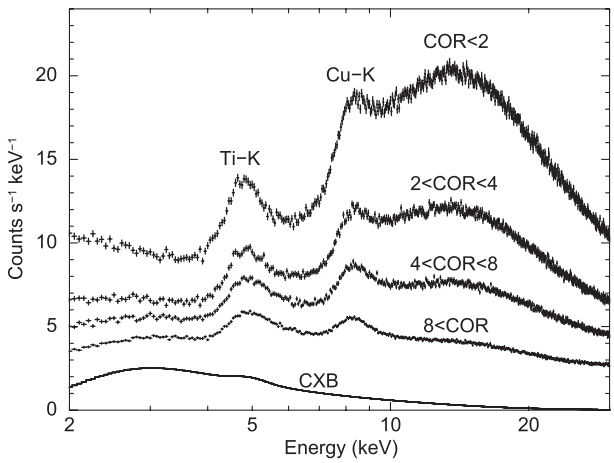


**Fig. 4.** GSC background spectra per counter sorted by COR (Cutoff Rigidity) and estimated contribution of the CXB (Cosmic X-ray Background). The data are average spectra of the entire 12 counters taken for a day on 2009 August 18. Ti-K and Cu-K fluorescent lines are seen at 4.6 keV and 8.1 keV, respectively.

The shape of the continuum in the energy band above 8 keV is quite sensitive to the COR. This suggests that the origins of these components would be energetic cosmic rays. The CXB component is expected to be dominant in the energy band below 5 keV at COR $>$ 8.

Figure 5 illustrates the background spectrum normalized by the effective area, and those of the Ginga LAC (Hayashida et al. 1989) and the RXTE PCA (Jahoda et al. 2006), where the expected contributions of the CXB in each instrument are included. Crab-like source spectra are shown together as a comparison. The GSC background is approximately 2 mCrab at 4 keV and 10 mCrab at 10 keV. The level is almost comparable to that of the Ginga LAC and slightly higher than that of the RXTE PCA.

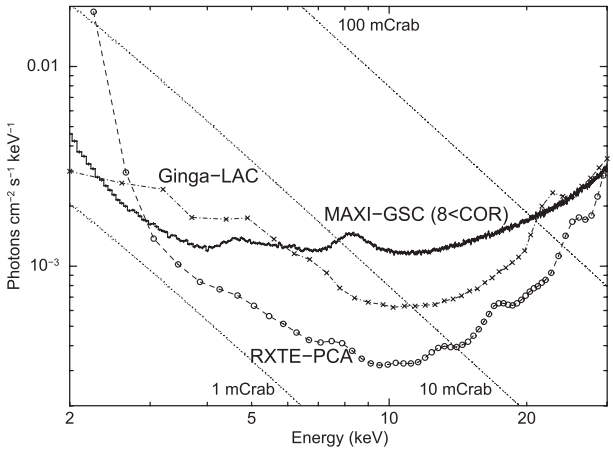


**Fig. 5.** GSC background energy spectrum normalized by the effective area and a comparison with those of Ginga-LAC, RXTE-PCA, and Crab-like source spectra. Expected contributions of the CXB in each instrument are included.

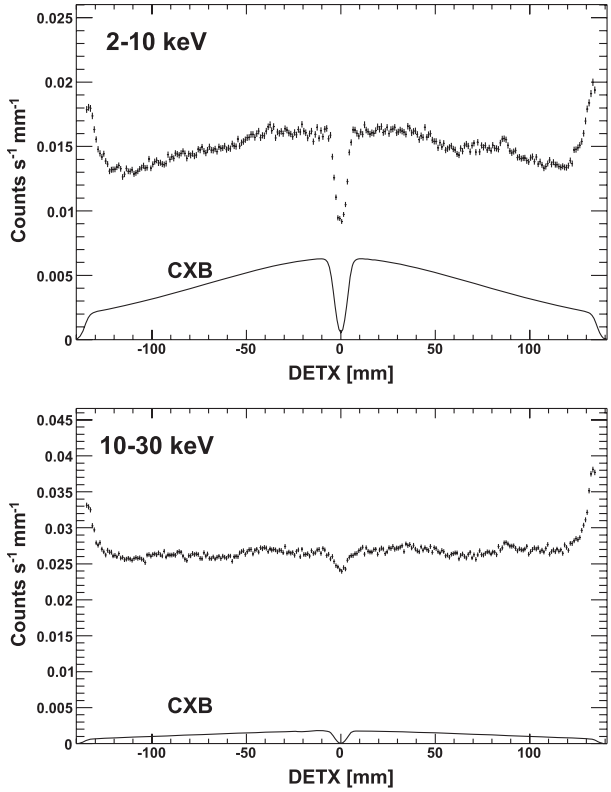


**Fig. 6.** Background spatial distribution in GSC gas counters along the anode wires (DETX) in each energy band of 2–10 keV (top) and 10–30 keV (bottom). Estimated contributions of the CXBs are shown with solid lines. The dips at the center (DETX $=$ 0) are due to the shadow of the support structure of the counter beryllium window.

### *3.1.3. Spatial distribution*

Figure 6 shows the spatial distributions of the residual backgrounds along the anode wire in 2–10 and 10–30 keV energy bands and the estimated contributions of the CXB. Each GSC counter has a sensitivity gap at the center of the anode wire due

to the frame structure used to support a 0.1-mm thick beryllium window. It causes a dip at the center in the spatial distribution. The depth of the dips can be mostly explained by extinction of the CXB component at the support structure.

The profile of the residual background left after subtracting the CXB component is primarily flat and slightly increases at both ends of the anode wires. This is because the efficiency of the anti-coincidence reduction decreases at the counter edge. The sensitivity is expected to get worse in these areas.

### 3.2. Energy Response and Gain Stability

Each gas counter is equipped with a calibration source embodying the radioactive isotope $^{55}$Fe at the end of one of six carbon anodes (the left-side end of carbon anode #2). It always exposes a collimated X-ray beam with a diameter of 0.2 mm. The counter gas gain and the energy resolution have been continuously monitored with the 5.9-keV line since a ground calibration test. The results show that the gas gain is stable within 2%, which agrees well with the results of a vacuum-environment test conducted on the ground. The variation in the orbit during the first year was within 0.8%. The energy resolution of 18% at 5.9 keV was stable within the statistical uncertainty.

The energy scale of the PHA of all the read-out signals were monitored at all locations along the carbon-anode wire using Ti-K and Cu-K fluorescent lines in the background, as can be seen in figure 4. The time variations for the first year were within 1% in the entire counter area. This information is employed for a PHA-to-PI (Pulse-height Invariant) conversion in the data-reduction process.

### 3.3. Detector Position Response and Stability

The incident X-ray position along a carbon-anode wire is calculated from the PHA ratio of two read-out signals to both anode ends. All of the required calibration data used to derive the detector position from the PHA ratio were collected in ground tests (Mihara et al. 2011).

The stability of the detector position response has been monitored with the calibration source since the ground calibration tests. The time variation of the calculated position during the first year was less than 0.2 mm, which corresponds to an angular distance of 0.°07 on the sky. It is small enough for the position determination accuracy of 0.°2 achieved. The detector position resolution of 2.0 mm (FWHM) for 5.9-keV X-rays at the nominal anode voltage of 1650 was constant within the statistical uncertainty of 0.05 mm ($1\,\sigma$) since the ground tests.

### 3.4. Point Spread Function in the Anode-Wire Direction

The point spread function (PSF) of the GSC is determined by the angular response of the slit-and-slat collimator and the position response of the position-sensitive gas counter along the anode wire. The collimator is designed to have an angular resolution of 1.°0–1.°5 in FWHM, which slightly depends on the X-ray incident angle. The position resolution of the gas counter depends on the X-ray energy. The resolution for X-rays with a normal incident angle is inversely proportional to the number of multiplied signal charges, and varies from 4 to 1 mm in the GSC energy band from 2 to 30 keV (Mihara et al. 2011). For events with slant incident angles, the variation of the photon-absorbed depth in a gas cell can also degrade the position resolution. The relation between the positional scale on the detector and the angular distance on the sky also depends on the incident angle. Thus, the PSF is represented by a complex function of X-ray energy and incident angle.

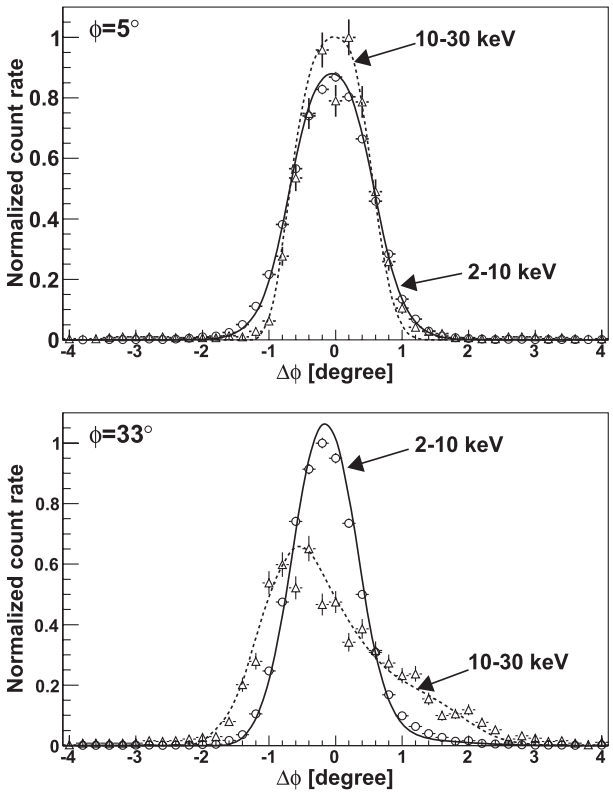


**Fig. 7.** PSF cross-section profiles along the detector anode-wire direction at each source-incident angle, $\phi$, of 5° (top) and 33° (bottom) in two energy bands of 2–10 keV (solid line) and 10–30 keV (dashed line). The power-law energy spectrum of photon index, 2.1, is assumed. Actual observed profiles of Sco X-1 taken at each source angle are plotted with 1-$\sigma$ error bars in the 2–10 keV (circle) and 10–30 keV (triangle) bands.

Figure 7 illustrates the cross-section profiles of PSF models for the direction along the detector anode-wire at each photon-incident angle, $\phi$, of 5° and 33° in 2–10 keV (soft) and 10–30 keV (hard) energy bands (see the geometry in figure 1). We also show the actual observed profiles taken from the data of a bright X-ray source, Sco X-1, for a comparison. The PSF models agree with the data within the statistical uncertainty. For events of $\phi = 5°$, which is close to the normal incident angle, the angular resolution in the hard band is better than that in the soft band, according to the better detector position resolution along the anode wire for the higher-energy X-rays. For events with a slant incident angle of $\phi = 33°$, the variation of the absorbed depth yields the broad distribution along the anode wire and degrades the resolution, especially in the hard band.

### 3.5. Scan Transit Profile and PSF in the Scan Direction

The GSC typically scans a point source on the sky during a transit of 40–150 seconds with a FOV of 1.°5-width (FWHM)

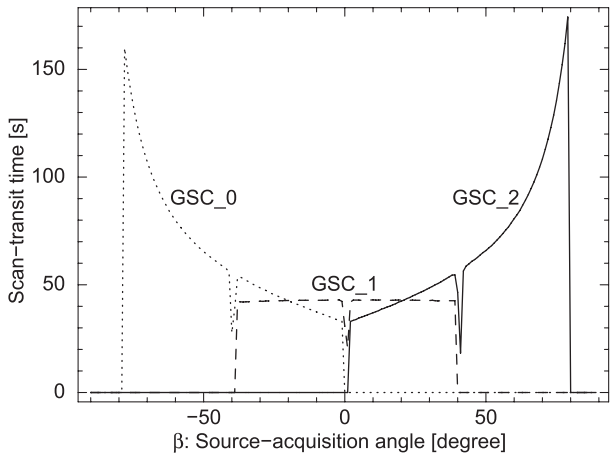


**Fig. 8.** Scan-transit time as a function of the source-acquisition angle for each GSC unit of GSC_0, GSC_1, and GSC_2, in the ISS normal attitude.

every 92-minute orbital period. The transit time depends on the source incident angle for each GSC counter, $\phi$, as well as the acquisition angle from the ISS rotation equator, $\beta$ (see the geometry in figure 1). Figure 8 illustrates the relation between the scan-transit time on each GSC counter and the source acquisition angle from the rotation equator in the ISS normal attitude. The scan duration increases from the ISS rotation equator ($\beta = 0°$) towards the pole ($\beta = \pm 90°$) in the side cameras, such as GSC_0 and GSC_2, according to the FOV-area angle from the rotation pole.

The detector area for the target changes according to the triangular transmission function of the collimator during each transit. It modulates time variations of the observed photon count rates, and represents the PSF in the scan direction if the source flux is constant. The scan direction is perpendicular to the detector anode-wire direction in the normal ISS attitude. Figure 9 shows time variations of the effective areas during scan transits at typical two source-acquisition angles of 5° and 72°, where the angular scales of the collimator transmission function are also indicated at the top on each panel. The observed count rates of Sco X-1 taken at the same acquisition angle are plotted together for a comparison. The calculated scan duration and the observed period agreed well with each other.

### *3.6. Exposure Map and Sensitivity*

An exposure map on the sky for a given period is calculated from the counter HV-operation history, the detector effective area as a function of a photon incident angle, and information of the ISS orbit, attitude, and configuration parameters interfering the FOV, such as the solar paddles, the space-shuttle vehicle docked on the ISS. Figure 10 shows actual exposure maps by all operated GSC counters for 92 minutes of an ISS-orbital cycle, one day, and 27 days since 2010 January 2, 00:00 (UT), calculated from all of the required information during these periods. GSC covers approximately 85% of the whole sky for one orbit, except for the orbits including the SAA passage, and 95% for a day. The daily map has uncovered the area for the Sun direction, the solar-paddle shadow, and

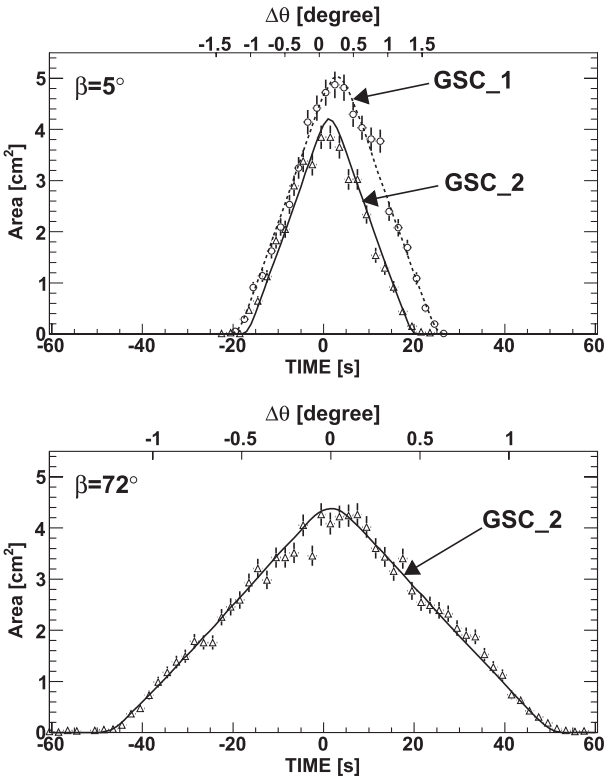


**Fig. 9.** Time variation of the effective area during each scan transit at a source-acquisition angle of 5° for GSC_1 and GSC_2 units (top) and 72° for GSC_2 units (bottom). The angular scale of each transit is shown at the top of each panel. The observed raw event rates of Sco X-1 by each GSC unit are plotted together with 1-$\sigma$ error bars.

the rotation pole that drifts on the sky according to the precession of the ISS orbit. We can achieve 100% full coverage within every three weeks.

The actual exposure time for an arbitrary direction on the sky was typically 4000 $cm^2$ s per day. This is about one third of the initial expectation because the HV operation at the high latitude above 40° was stopped and four counters out of 12 were disabled during this period. The daily 5-$\sigma$ source sensitivity is expected to become 15 mCrab, which is three-times worse than that of the pre-flight simulation (Matsuoka et al. 2009).

## 4. Calibration Status

We here present the status of the GSC response calibration for data taken at the nominal HV of 1650 V. We also exclude data detected by anodes #1 and #2 of all GSC counters because some of them show complicated energy–PHA relations at low PHA, which is probably due to feedback crosstalks on the circuit board. The responses functions for the data taken at the reduced HV of 1550 V and by the anodes #1 and #2 are being developed, and will be updated soon.

### *4.1. Alignment and Position Localization Accuracy*

The attitude of the MAXI payload module is continuously measured with the on-board Attitude Determination System (ADS), which consists of a Visual Star Camera (VSC) and

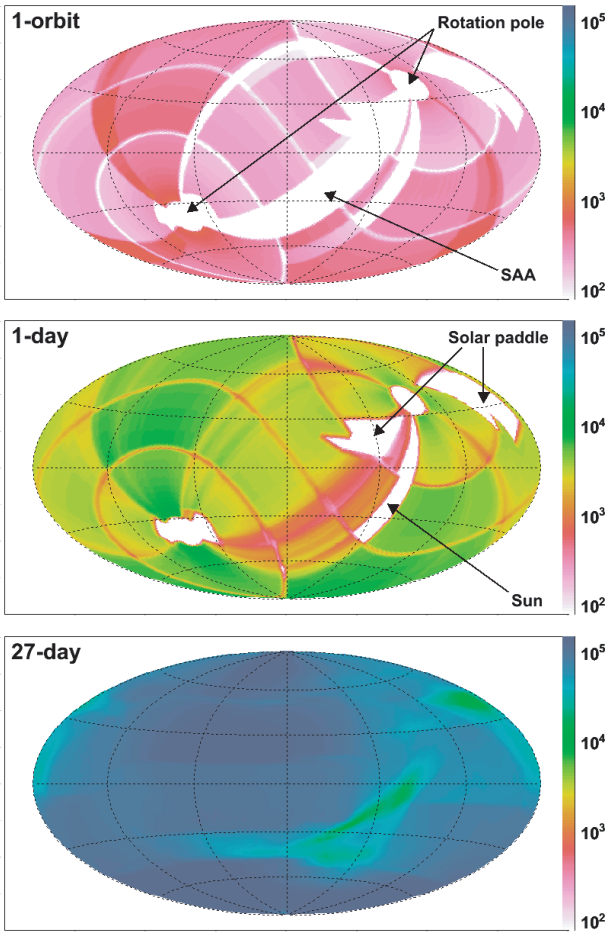


**Fig. 10.** GSC exposure map by scans of 92-minute orbital period (top), 1 day (middle), and 27 days (bottom) since 2010 January 2 00:00 (UT). The color scales of all three panels are identical, and represent the effective exposure for the sky direction in the units [$\mathrm{cm}^2$ s]. The uncovered areas for the rotation pole, the Sun direction, the SAA, and the interference with the solar paddles are indicated with arrows.

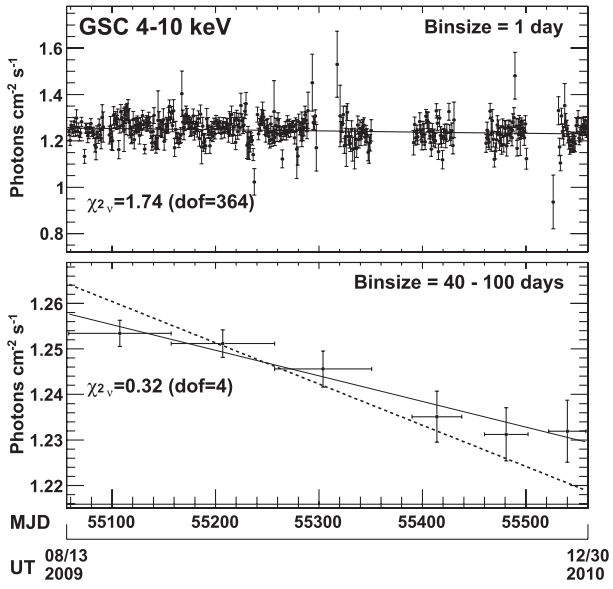


**Fig. 11.** (Top) Crab nebula light curve by GSC in 4–10 keV band in one-day time bin. The vertical errors represent the 1-$\sigma$ statistical uncertainties. Solid line represents the best-fit linear model. The reduced chi-square ($\chi^2_\nu$) and the degrees of freedom (DOF) of the fit is shown on the panel. (Bottom) The same Crab nebula light curve, but in 40–100-day time bin and the best-fit linear model. The model with a slope extrapolated from the 5.1% decline from MJD 54690 to 55435 observed by RXTE/PCA in 2–15 keV band (Wilson-Hodge et al. 2011) is shown together with dashed line.

a Ring Laser Gyroscope (RLG). Its accuracy is estimated to be better than an arc minute from ground calibration tests (Horike et al. 2009). The source location of an incident X-ray on the sky is calculated from the position coordinates on the detector where the X-ray is absorbed and the attitude parameters at the event time. The alignments of the collimators and detectors on the payload module are calibrated using standard X-ray sources whose positions and intensities are well-known. The accuracy of 0.°2 in the 90% containment radius of the best determined position has been confirmed so far using several bright-source samples selected randomly (Morii et al. 2011).

### 4.2. *Effective Area and Light Curve*

The visibility and the area of each GSC unit for a given X-ray source on the sky are always changing according to the ISS orbital motion and interferences with other relevant ISS activities, as shown in subsection 3.5. To derive the intrinsic time variation of a certain X-ray source, the time-dependent effective area for the target has to be known. The light-curve response builder calculates the area curve of each GSC unit from the source coordinates, the ISS location, attitude, and the area of the GSC unit as a function of the source incident angle. The areas of all the GSC units were calibrated on the ground using pencil X-ray beams (Morii et al. 2006).

The top panel of figure 11 shows the obtained light curve of the Crab nebula in the 4–10 keV energy band since the mission started on 2009 August 15. The data have been collected from the area-corrected photon count rates for each day. Backgrounds are estimated from the count rates for the adjacent sky region, which corresponds to the data obtained from the successive time periods. A power-law energy spectrum with a photon index, $\Gamma = 2.1$, is assumed in the effective-area correction. The light curve should be approximately constant and consistent with the flux of the standard Crab model. The measured average flux over the entire period, 1.25 photons $\mathrm{cm}^{-2}\ \mathrm{s}^{-1}$, agrees with the standard Crab value (Kirsch et al. 2005; Weisskopf et al. 2010). However, the fit to a linear model results in a reduced chi-squared $\chi^2_\nu = 1.74$ for 364 degrees of freedom (DOF), which is not accepted within the 90% confidence limit. This is due to the limit on the effective-area calibration accuracy on a daily basis. The error on the daily flux in the 4–10 keV band is estimated to be 3% with the 1-$\sigma$ range. A calibration over the entire 2–30 keV energy range is in progress.

Recently, Wilson-Hodge et al. (2011) presented evidence of flux variations of the Crab nebula by $\sim$7% on a 3-year timescale, consistently observed by Fermi/GBM, RXTE/PCA, Swift/BAT, and INTEGRAL/ISGRI. The flux in the 2–15 keV band observed by RXTE/PCA exhibits a 5.1% decline from

MJD 54690 to 55435. We examined the variation with the GSC data. The bottom panel of figure 11 shows the variation in the obtained GSC 4–10 keV flux by each interval of about 100 days. The start and the end of each interval are slightly adjusted according to the observation-time coverage. A continuous decline is clearly seen. The fluxes averaged by the long term are derived from large event data taken at various camera angles and detector positions. Therefore, the calibration uncertainty of the effective area on a daily basis, 3% in $1\sigma$, is supposed to be smeared out in it, and the observed decline is considered to be real.

We fitted the data to a linear function, and obtained a decline ratio of $2.2\% \pm 0.5\%$ (1-$\sigma$ statistical uncertainty) from MJD 55058 to 55558. The ratio is slightly smaller than that extrapolated from the 5.1% decline in MJD 54690–55435 observed by the RXTE/PCA in 2–15 keV band. We tried to fit the GSC data to a linear model with the fixed slope determined by the RXTE/PCA, as shown in figure 11. The fit is marginally unacceptable with $\chi^2_\nu = 1.92$ for 5 DOF. This might imply the dependence of the variation amplitude on the energy band, as reported in Wilson-Hodge et al. (2011).

### 4.3. Energy Response Matrix

The energy response matrix is represented by the product of the effective area and the dispersion relation between the incident X-ray energy and the PHA of the output signal. The dispersion relation as well as the gas gain depend on the 3-dimensional location where the X-ray photon is absorbed in a detector gas cell. The spatial gain variation and the time variation in orbit are corrected event by event in the first data-reduction process using calibration data collected from the ground and in-orbit test results. All of the dispersion relations required to derive the response matrix were taken in the ground test (Mihara et al. 2002).

The energy response builder calculates the effective area and the energy redistribution matrix for a target source at given sky coordinates during a given observation period. The program accumulates instantaneous response functions for the source location according to the variation of the incident angle during the active observation period.

Figure 12 shows a Crab spectrum by GSC taken for a day on 2009 August 15 (UT) and the best-fit power-law model with interstellar absorption, folded by the response matrix obtained by the response builder. Backgrounds are extracted from events in the adjacent sky region. The best-fit parameters are summarized in table 1. The model-to-data ratio shows that the obtained spectrum is well reproduced within 10% over the 2–30 keV energy range. The best-fit absorption column density, $(0.72 \pm 0.22) \times 10^{22}\,\mathrm{cm}^{-2}$, is slightly higher than the standard Crab value, $0.35 \times 10^{22}\,\mathrm{cm}^{-2}$ (Kirsch et al. 2005), although the fit with the absorption fixed at the standard value is also accepted within the 90% confidence limit. The discrepancy is considered to be due to the inaccuracy of the effective-area calibration at the low-energy band. The fine calibration is in progress.

### 4.4. Timing

In-orbit timing calibrations are performed using signals from X-ray pulsars or binaries, such as the Crab pulsar and Cen X-3 with 33 millisecond and 4.8 second periods, respectively. Events within the PSF of these pulsars are extracted and applied to the barycentric correction. The pulsation of Crab pulsar can be detected for every one-day interval. Figure 13 shows the folded pulse profiles since 2010 January 1 to January 5. The absolute timing and the relative stability are estimated by the relative pulse phase of the Crab pulsar to those with the radio wavelength (Lyne et al. 1993) and RXTE/PCA (Rots et al. 2004), and comparison of the Cen X-3 pulse period and phase with those of the Fermi/GBM (Meegan et al. 2009). We confirmed a timing stability on the order of $10^{-9}$.

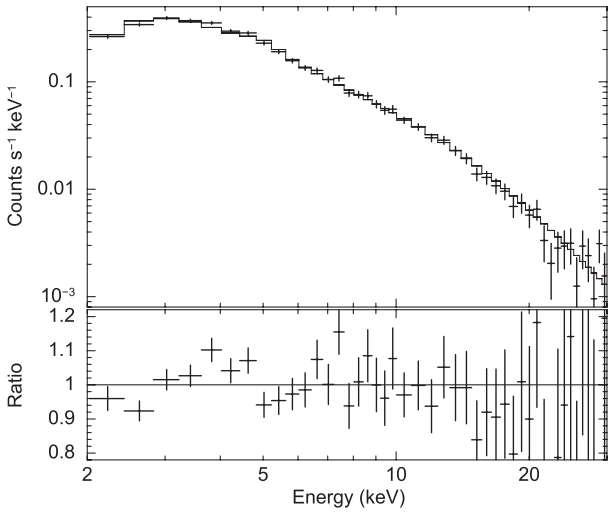


**Fig. 12.** GSC Crab-nebula spectrum taken for a day on 2009 August 15 (UT) and the best-fit power-law model with a fixed absorption of $0.35 \times 10^{22}\,\mathrm{cm}^2$ (top). Data-to-model ratio (bottom).

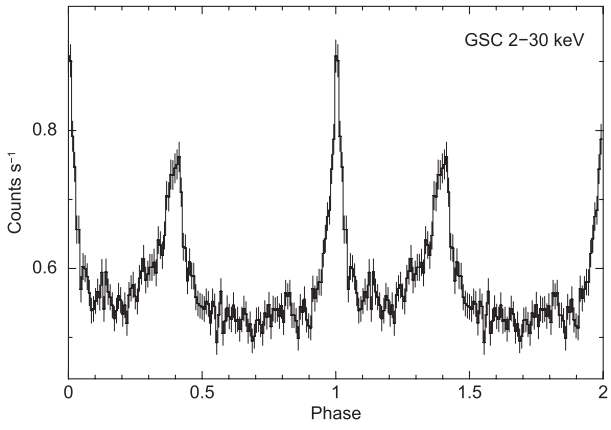


**Fig. 13.** Folded light curve of the Crab pulsar in 2–30 keV band obtained with GSC during the period from 2010 January 1 to January 5. The vertical count rate represents the event rate from the target direction over the entire elapsed period.

## 5. All-Sky Image

Figure 14 shows the GSC all-sky X-ray image taken for the first year. The red, green, and blue color scales represent the intensity in the 2–4, 4–8, and 8–20 keV energy bands,

**Table 1.** Best-fit parameters for GSC Crab-nebula spectrum.*

| Model | $N_{\rm H}$† | $\Gamma$‡ | Normalize§ | $\chi^2_\nu$ (DOF) |
|---|---|---|---|---|
| Power-law, $N_{\rm H}$: free | $0.72 \pm 0.22$ | $2.15 \pm 0.05$ | $11.4 \pm 1.0$ | 1.08 (43) |
| Power-law, $N_{\rm H}$: fixed | 0.35 | $2.08 \pm 0.03$ | $9.9 \pm 0.4$ | 1.25 (44) |

* All errors represent 90% confidence limits of statistical uncertainty.
† Absorption hydrogen column density in units of $10^{22}\,{\rm cm}^{-2}$.
‡ Power-law photon index.
§ Power-law normalization in units of photons ${\rm cm}^{-2}\ {\rm s}^{-1}\ {\rm keV}^{-1}$ at 1 keV.

**Fig. 14.** GSC all-sky image taken for the first year. Red, green, and blue color maps are scaled logarithmically and represent the intensities in 2–4, 4–8, and 8–20 keV bands, respectively.

**Table 2.** Summary of GSC in-orbit performance.

| | |
|---|---|
| Spatial resolution | 1.°5 (FWHM) |
| Source localization accuracy | $0 \pm 2$ (90% containment radius) |
| All-sky coverage | 85% per orbit (nominal 92 minutes), 95% per day |
| Exposure | 4000 ${\rm cm}^2$ s per day (typical) |
| Energy resolution | 18% ($1\,\sigma$) at 5.9 keV |
| Effective area accuracy | 3% ($1\,\sigma$) at 4–10 keV |
| Sensitivity | 15 mCrab per day in 2–30 keV (typical) |

respectively. The diameter of point-source images roughly represents the relative brightness according to the PSF spread. We can easily see more than a hundred discrete X-ray sources over the whole sky as well as unresolved Galactic ridge emission along the Galactic plane with a scale height of 1°–2°.

## 6. Summary

The GSC in-orbit performance on the MAXI mission payload has been verified from the initial commissioning operation. Table 2 briefly reviews the relevant parameters. They are summarized by the following points:

1. The optimal configurations of the read-out electronics and on-board data processing at the nominal high voltage of 1650 V have been established. The gas gain and the amplifier gain have been confirmed to agree with those expected from the ground calibration tests. The gain change during the first year is confirmed to be less than 1%, which is small enough for the requirements of the calibration accuracy.
2. Two gas counters out of the twelve were turned off for the high-voltage breakdown during the first two-months commissioning operation, and another breakdown occurred in the ninth month. These breakdowns

would be presumably caused by repeated discharges. The HV operation under the high particle-background, which includes the area at high latitude above 40° as well as the SAA, were stopped since 2009 September 27 in order to avoid any damage that could develop into discharges. The three counters suffering from the breakdown are now operated with a limited sensitivity using alive-anode partitions.

3. The background cosmic-ray rate is consistent with that extrapolated from past experiments in low-Earth orbit using the relation with the geomagnetic COR. The efficiency of the on-board background rejection by the anti-coincidence-hit logic is also found to be comparable to those of similar instruments, Ginga-LAC.
4. The PSF with an FWHM of 1°.5, the scan transit time from 40 to 150 seconds per orbital cycle, the all-sky coverages of 85% per 92-minute orbital period and 95% per day have been verified, which agrees with the pre-flight design. The effective exposure time for a celestial target is typically 4000 $cm^2$ s. The daily 5-$\sigma$ source sensitivity is expected to be 15 mCrab under the condition.
5. The instrument response in orbit has been calibrated using Crab nebula data. The fitting results verified that the uncertainty of the effective area and the energy response would be less than 10% if data of a few anodes suffering from cross talk on the circuit board are ignored. The relative timing accuracy was also confirmed to be normal.

We are grateful to Mark Finger and the Fermi/GBM pulsar project team for providing the pulsar ephemeris data for timing calibration. We also thank Keith Jahoda for stimulating and constructive comments. This research was partially supported by the Ministry of Education, Culture, Sports, Science and Technology (MEXT), Grant-in-Aid for Science Research 19047001, 20244015, 21340043, 21740140, 22740120 and Global COE from MEXT "Nanoscience and Quantum Physics" and "The Next Generation of Physics, Spun from Universality and Emergence".

## References

Gendreau, K. C., et al. 1995, PASJ, 47, L5
Hayashida, K., et al. 1989, PASJ, 41, 373
Horike, N., Maeda, K., & Ueno, S. 2009, in Proc. Astrophysics with All-Sky X-Ray Observations, ed. N. Kawai (Wako, Saitama: RIKEN), 24
Jahoda, K., Markwardt, C. B., Radeva, Y., Rots, A. H., Stark, M. J., Swank, J. H., Strohmayer, T. E., & Zhang, W. 2006, ApJS, 163, 401
Kirsch, M. G., et al. 2005, Proc. SPIE, 5898, 589803
Kokubun, M., et al. 2007, PASJ, 59, S53
Lyne, A. G., Pritchard, R. S., & Smith, F. G. 1993, MNRAS, 265, 1003
Makishima, M., et al. 1996, PASJ, 48, 171
Matsuoka, M., et al. 2009, PASJ, 61, 999
Meegan, C., et al. 2009, ApJ, 702, 791
Mihara, T., et al. 2002, Proc. SPIE, 4497, 173
Mihara, T., et al. 2011, PASJ, 63, S623
Morii, M., et al. 2006, Proc. SPIE, 6266, 62663U
Morii, M., Sugimori, K., Kawai, N., & the MAXI Team 2011, Physica E, 43, 692
Rots, A. H., Jahoda, K., & Lyne, A. G. 2004, ApJ, 605, L129
Tomida, H., et al. 2011, PASJ, 63, 397
Tsunemi, H., Tomida, H., Katayama, H., Kimura, M., Daikyuji, A., Miyaguchi, K., Maeda, K., & the MAXI Team 2010, PASJ, 62, 1371
Turner, M. J. L., et al. 1989, PASJ, 41, 345
Weisskopf, M. C., Guainazzi, M., Jahoda, K., Shaposhnikov, N., O'Dell, S. L., Zavlin, V. E., Wilson-Hodge, C., & Elsner, R. F. 2010, ApJ, 713, 912
Wilson-Hodge, C. A., et al. 2011, ApJ, 727, L40